



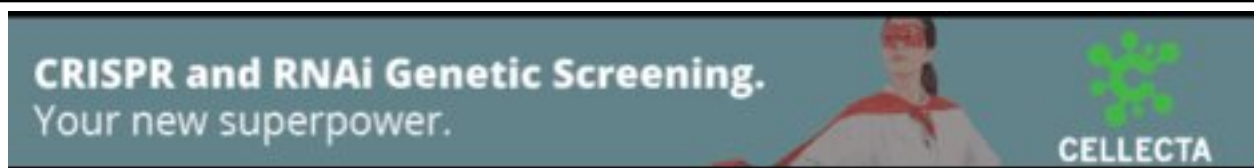
Profiling single-cell histone modifications using indexing chromatin immunocleavage sequencing

Wai Lim Ku, Lixia Pan, Yaqiang Cao, et al.

Genome Res. published online April 14, 2021

Access the most recent version at doi:[10.1101/gr.260893.120](https://doi.org/10.1101/gr.260893.120)

P<P	Published online April 14, 2021 in advance of the print journal.
Accepted Manuscript	Peer-reviewed and accepted for publication but not copyedited or typeset; accepted manuscript is likely to differ from the final, published version.
Open Access	Freely available online through the <i>Genome Research</i> Open Access option.
License	This is a work of the US Government.
Email Alerting Service	Receive free email alerts when new articles cite this article - sign up in the box at the top right corner of the article or click here .



To subscribe to *Genome Research* go to:
<https://genome.cshlp.org/subscriptions>

Published by Cold Spring Harbor Laboratory Press

Profiling single-cell histone modifications using indexing chromatin immunocleavage sequencing

Wai Lim Ku^{1,2}, Lixia Pan^{1,2}, Yaqiang Cao¹, Weiwu Gao¹, Keji Zhao^{1,*}

1. *Laboratory of Epigenome Biology, Systems Biology Center, National Heart, Lung and Blood Institute, NIH, Bethesda, MD, USA*

2. *These authors contributed equally to this work.*

**Corresponding author.*

Keji Zhao

Email : zhaok@nhlbi.nih.gov

Phone: 301-496-2098

Fax : 301-402-0971

ABSTRACT

Recently, multiple single cell assays were developed for detecting histone marks at the single cell levels. These techniques are either limited by the low cell throughput or sparse reads which limit their applications. To address these problems, we introduce indexing single-cell immunocleavage sequencing (iscChIC-seq), a multiplex indexing method based on TdT terminal transferase and T4 DNA ligase mediated barcoding strategy and single-cell ChIC-seq, which is capable of readily analyzing histone modifications across tens of thousands of single cells in one experiment. Application of iscChIC-seq to profiling H3K4me3 and H3K27me3 in human white blood cells (WBCs) enabled successful detection of more than 10,000 single cells for each histone modification with 11K and 45K non-redundant reads per cell, respectively. Cluster analysis of these data allowed identification of monocytes, T cells, B cells, and NK cells from WBCs. The cell types annotated from H3K4me3 single cell data are specifically correlated with the cell types annotated from H3K27me3 single cell data. Our data indicate that iscChIC-seq is a reliable technique for profiling histone modifications in a large number of single cells, which may find broad applications in studying cellular heterogeneity and differentiation status in complex developmental and disease systems.

57

58 **Introduction**

59 Histone modifications, which are typically measured by chromatin immunoprecipitation (ChIP) with massively
60 parallel DNA sequencing (Barski et al. 2007; Johnson et al. 2007; Mikkelsen et al. 2007; Robertson et al. 2007)
61 at the bulk-cell level, are associated with transcriptional regulation. Chromatin regions enriched in H3K4
62 methylation and H3K27 acetylation are potentially active promoters or enhancers that activate the transcription
63 of target genes; on the other hand, genes enriched in H3K27me3 signals are usually repressed (Kim et al. 2005;
64 Barski et al. 2007; Mikkelsen et al. 2007; Wei et al. 2009; Creyghton et al. 2010). While the genomic profiles of
65 various histone modifications have been extensively characterized at the bulk cell level, several single-cell
66 epigenomic techniques for detecting histone modification marks are reported recently (Rotem et al. 2015; Ai et
67 al. 2019; Carter et al. 2019; Grosselin et al. 2019; Hainer et al. 2019; Harada et al. 2019; Kaya-Okur et al. 2019;
68 Ku et al. 2019; Wang et al. 2019).

79

80 Although single cell assays including scChIL-seq (Harada et al. 2019), scChIC-seq (Ku et al. 2019),
81 uliCUT&RUN (Hainer et al. 2019), scCUT&Tag (Kaya-Okur et al. 2019), iACT-seq (Carter et al. 2019),
82 CoBATCH (Wang et al. 2019), itChIP-seq (Ai et al. 2019) and scChIP-seq (Rotem et al. 2015; Grosselin et al.
83 2019) were developed recently for measuring histone marks (**Supplemental Table S1**), they have specific
84 limitations. While scChIP-seq combined the droplet barcoding approach with ChIP-seq (Barski et al. 2007;
85 Rotem et al. 2015; Grosselin et al. 2019), all other methods except for itChIP-seq replaced the traditional
86 immunoprecipitation with antibody guided digestion of chromatin either via antibody-directed, transposase-
87 mediated integration of a DNA tag and fragmentation (for scChIL-seq (Harada et al. 2019) and
88 scCUT&Tag (Kaya-Okur et al. 2019), iACT-seq (Carter et al. 2019), CoBATCH (Wang et al. 2019)), or via DNA
89 cleavage specifically around nucleosomes containing the target modification (Schmid et al. 2004) (for
90 uliCUT&RUN (Hainer et al. 2019) and scChIC-seq (Ku et al. 2019)). scChIP-seq (Rotem et al. 2015; Grosselin et
91 al. 2019), with a relatively complicated workflow, could detect about 2000-4000 cells in one experiment with
92 an average of 4000 reads per cell. Although iACT-seq, scCUT&Tag, uliCUT&RUN, itChIP-seq and scChIC-
93 seq have simpler workflows and more cost-effective, iACT-seq and scCUT&Tag could detect an average of
94 2000-6000 reads per cells and the cell throughput of uliCUT&RUN, itChIP-seq and scChIC-seq is low. While
95 scChIL-seq and CoBATCH worked well for detecting active marks, they were not optimal for detecting
96 repressive marks in fixed samples considering the attenuated activity of Tn5 in non-accessible chromatin
97 regions and its intrinsic bias towards open regions (Harada et al. 2019). Therefore, there is a need to develop a
98 single cell technique for profiling histone marks with higher cell throughput, more widely applications and
99 detection of more reads per cell.

100

Results

The simultaneous addition of several dG nucleotides to DNA ends by TdT enzyme and ligation of oligo-dC barcode adaptors by T4 DNA ligase is an efficient strategy to barcode chromatin regions following DNase digestion. We adapted this barcoding strategy to label the DNA ends generated by antibody-guided MNase cleavage in ChIC-seq assays to profile histone modifications in more than tens of thousands of single cells in one experiment through three levels of barcoding and indexing strategy (**Fig. 1A-B**). Briefly, following antibody-guided MNase digestion of cells cross-linked with formaldehyde and disuccinimidyl glutarate (DSG), several dGs were added to the DNA ends by the activity of TdT in the presence of T4 DNA ligase and oligo-dC barcode adaptors in a 96-well plate. The cells were then pooled from 96 wells and aliquoted into new 96-well plates with 30 cells per well by flow cytometry sorting, followed by two consecutive rounds of PCR amplification. The samples were then pooled, purified, and sequenced using Illumina HiSeq 3000. The barcodes and PCR indexes (**Supplemental Table S2**) were identified and resolved to reveal single cells using a previous strategy (Cusanovich et al. 2015).

We first examined the collision rate by applying iscChIC-seq to a mixture of mouse NIH3T3 and human HEK293T cells. We found that reads from cells were mainly mapped either to the mouse genome (n=439) or the human genome (n=2,371), while 149 barcodes were categorized as human and mouse doublets. The human-mouse cell doublet rate is approximately 10% (**Supplemental Fig. S1; Methods**), which is similar to the collision rate of 12% obtained from the estimation based on the number of cells per well (Rubin et al. 2019). We then applied iscChIC-seq to white blood cells isolated from human blood for profiling the H3K4me3 modification, which is an active histone modification mark, at a single cell resolution. Using a cutoff to filter cells with less than 1,000 reads, we detected 10,000 single cells and about 9,000 reads per cell on average in one single experiment (**Supplemental Table S3**). Using a more stringent filtering criteria (a cell has at least 3,000 reads), this resulted in ~7,800 single cells each having about 11,000 reads on average. Note that the number of total reads in some wells of the PCR plate are much lower than other wells (**Supplemental Table S3**), which could be caused by the irregularities of the PCR machine, for example, temperature control at those few wells. The cell number and unique reads number per cell detected by iscChIC-seq are significantly improved as compared with the previous published single-cell methods (**Supplemental Table S3**), while the precision of reads detected by iscChIC-seq is comparable to other methods (Grosselin et al. 2019; Kaya-Okur et al. 2019). The duplication rate of iscChIC-seq reads is about 73% while it is 87% for scCUT&Tag (Kaya-Okur et al. 2019) and 23% for scChIP-seq (Grosselin et al. 2019). The genomic profiles of the sequencing read from pooled single cells displayed specific peaks around transcription start site (TSS) and were highly consistent with that of the bulk cell H3K4me3 ChIP-seq data from ENCODE (**Fig. 2A; Supplemental Fig. S2A, B**). Using

35 SICER(Zang et al. 2009; Xu et al. 2014), 36,169 H3K4me3 peaks were detected from the pooled single cells.
36 Using a similar strategy, 52,798 H3K4me3 peaks were detected from the ENCODE ChIP-seq data from
37 different immune cells in human WBCs (**Supplemental Table S4**). Comparison of the ENCODE data with our
38 single-cell data revealed that 31,432 out of 36,169 (87%) H3K4me3 peaks from the pooled cells overlapped
39 with the peaks from the bulk cell H3K4me3 ChIP-seq data (**Fig. 2B**). The read densities of the pooled single
40 cells and the bulk cell ChIP-seq data were highly correlated ($r=0.89$) (**Fig. 2C**). Also, the pooled single cell data
41 showed high enrichment and nucleosome phasing around the transcription start site (TSS) (**Fig. 2D**), as found
42 from ChIP-seq data(Barski et al. 2007). Together, these results indicate that our iscChIC-seq data can
43 effectively detect H3K4me3 marks in single cells.

44
45 To further study the performance of iscChIC-seq, we compared the sensitivity (i.e., percentage of true peaks
46 recovered) and precision (i.e., percentage of reads located in true peaks) of iscChIC-seq to both scCUT&Tag
47 (Kaya-Okur et al. 2019) and scChIP-seq(Grosselin et al. 2019). Note that H3K4me2 from scCUT&Tag was
48 compared to H3K4me3 from either iscChIC-seq and scChIP-seq due to the lack of published single cell
49 H3K4me3 data using scCUT&Tag. The results showed that iscChIC-seq has the best performance in sensitivity,
50 while its precision is either compatible with or slightly lower than scChIP-seq or scCUT&Tag (**Supplemental**
51 **Fig. S3**). To check the reproducibility of iscChIC-seq, we generated two sets of single cell H3K4me3 data. We
52 pooled the single cells in each set of data and compared the H3K4me3 density between the two pooled sets. The
53 results showed that the two replicates are highly correlated ($r=0.96$, **Supplemental Fig. S4**).

54
55 Next, we examined if different cell types of the human WBCs, which contain T cells, NK cells, monocytes, and
56 B cells, could be identified from the iscChIC-seq data. For this purpose, a combined reference set of H3K4me3
57 peaks for human WBCs were first computed using the ENCODE bulk cell H3K4me3 ChIP-seq data (**Methods**).
58 By applying the silhouette analysis(Rousseeuw 1987), a number of six were found to be the optimal number of
59 clusters (**Supplemental Fig. S5A; Fig. 3A**). To annotate the cells in each cluster, we pooled the cells from each
60 cluster and identified the H3K4me3 peaks that are specific to each cluster. Using the ENCODE T cell, B cell,
61 NK cell, monocyte bulk cell H3K4me3 ChIP-seq data, we identified the peaks that are specific to each cell type.
62 Next, the statistical significance of the overlap between the two types of specific peaks was calculated using
63 hypergeometric test, which robustly annotated four of the six clusters to be monocytes, T cells, B cells, and NK
64 cells while the other two clusters could not be clearly annotated (**Fig. 3A, B; Methods**). Sub-sampling using
65 33% of single cells from each cluster confirmed the accurate and reproducible annotation of these cells
66 (**Supplemental Fig. S5B; Methods**). From the four annotated clusters, 1,610 monocytes, 1,265 T cells, 898 NK
67 cells, and 446 B cells were obtained.

59 Next, we compared the genomic profiles of the annotated pooled single cell data (from cluster T, B, NK, and
60 monocyte) with the genome profiles of ENCODE bulk cell ChIP-seq data for the corresponding cell types. The
61 analysis revealed that the annotated cluster of single cells showed a genomic profile highly similar to that of the
62 corresponding bulk cells at the cell type-specific gene loci including *PAX5*, *CD19*, *CD14*, *CD93*, *CD3D*, *CD5*,
63 *TBX21* and *NCRI* (**Fig. 3C**). By comparing the cell type-specific peaks identified from the ENCODE data and
64 cluster-specific peaks identified from the pooled single cells, we found that about 80% to 90% of cell type-
65 specific peaks were detected in the pooled single cells from the NK, monocyte and T clusters while only 26% of
66 cell-specific peaks were detected in the pooled single cells from the B cluster (**Supplemental Fig. S6**), which
67 may be related to the relatively small number of cells in the B cluster. But, in all cases, much lower fractions of
68 cell type-specific peaks were detected from other cell types than the annotated cell type in the single-cell
69 cluster, indicating the signals from the pooled single cells are specific. Since H3K4me3 is an active mark, we
70 compared the expression levels of genes associated with the specific peaks identified in the pooled single cells
71 from each annotated cluster. The analysis indicated that the genes associated with cluster-specific peaks are
72 expressed at significantly higher levels in the annotated cell type than the other cell types (**Supplemental Fig.**
73 **S7**).

34
35 At the single cell level, the majority of cells annotated as T cells, B cells, NK cells, monocytes exhibited high
36 H3K4me3 density in regions associated with $CD3D^+CD3E^+CD3G^+$ (T cell-specific), *PAX5* (B cell-specific),
37 *TBX21* (NK and T cell-specific), $CD14^+CD93^+$ (monocyte-specific), respectively (**Fig. 3D**). Overall, these
38 results indicate that iscChIC-seq could reliably identify different cell types from a complex population of cells
39 such as WBCs. To estimate the minimum number of reads that was required for reliable clustering analysis, we
40 have subsampled the reads in single cell H3K4me3 data using different percentage (90%, 80%, 70%, 60%, and
41 50%) of reads from the original set of reads for each cell. An original cluster is considered to be successfully
42 recovered if there is only one new cluster that has more than 40% of cells overlap with that of the original
43 cluster. For H3K4me3, about 90% of reads were required in order to recover the original six clusters
44 (**Supplemental Figs. S8A and B**). Similarly, to estimate the minimum number of cells that was required for
45 reliable clustering analysis we have subsampled the cells in single cell H3K4me3 data using different
46 percentage (90%, 70%, 50%, 30%). We observed that about 50% of cells (3,000 cells) were required for
47 H3K4me3 single cell data to recover the six clusters (**Supplemental Fig. S8C and D**).

48
49 To test if iscChIC-seq works for detecting repressive histone marks, we applied it to profiling H3K27me3 in
50 WBCs. Using a filtering approach similar to that used for H3K4me3 iscChIC-seq libraries, we detected 10,000
51 single cells each having about 40,000 unique reads on average. Using a more stringent filtering criteria such that
52 a cell has at least 4,000 unique reads, it resulted in ~9,000 single cells each having about 45,000 reads on

average. The genomic profiles of the pooled single cells were highly consistent with the profiles of the bulk cell H3K27me3 ChIP-seq data from ENCODE (**Fig. 4A; Supplemental Fig. S9**). We detected a total of 79,110 and 35,246 enriched regions from the ENCODE bulk cell ChIP-seq data and the pooled single cell data, respectively. Comparison of the ENCODE data with our single-cell data revealed that 31,726 of 35,246 (90%) H3K27me3 peaks from the pooled single-cells overlapped with the peaks from the ENCODE H3K27me3 ChIP-seq data (**Fig. 4B**). The read densities of the pooled single cells and the bulk cell ChIP-seq data were highly correlated ($r=0.92$) (**Fig. 4C**). Applying the silhouette analysis to H3K27me3 iscChIC-seq data, an optimal number of clusters equal to six was found (**Supplemental Fig. S2C**), which was the same as the H3K4me3 iscChIC-seq data. Similar to the H3K4me3 data, the clustering analysis of the H3K27me3 iscChIC-seq data revealed six clusters of cells (**Fig. 4D, Methods**). After pooling the cells from each cluster, the cluster-specific peaks were identified and compared to the T cell, B cell, NK cell, monocyte specific peaks identified from the ENCODE bulk cell ChIP-seq data. Four cell clusters, including 1,146 T cells, 432 B cells, 749 NK cells, 2,192 monocytes, were annotated by the significant overlap between the two types of peaks (**Fig. 4E**). Similar to H3K4me3, we estimated the minimum of number of reads and cells that was required for reliable clustering analysis. We found that about 80% of reads for H3K27me3 were required in order to recover the original six clusters (**Supplemental Fig. S10A and B**) while about 70% of cells (4,900 cells) were required for H3K27me3 single cell data to recover the six clusters (**Supplemental Fig. S10C and D**). Overall, these results indicate that iscChIC-seq could also reliably profile repressive histone marks in a mixed population of cells.

Different from ChIP-seq, ChIC-seq depends on antibody-guided cleavage of chromatin by MNase and thus may have bias toward open chromatin regions. To address this question, we identified all the DHSs from the ENCODE DNase-seq datasets from T, B, NK and monocyte cells and analyzed the fraction of the ENCODE bulk cell H3K4me3 ChIP-seq reads that overlapped with DHSs in each cell type. The analysis revealed that about 60% to 67% of H3K4me3 ChIP-seq reads from the ENCODE bulk cell H3K4me3 ChIP-seq libraries fell into the DHS regions (**Supplemental Table S5A**). In contrast, about 52% to 56% of the H3K4me3 reads from the pooled single cells fell into the DHS regions (**Supplemental Table S5A**), suggesting that the specificity of the H3K4me3 reads from the iscChIC-seq libraries is slightly lower than that of the bulk cell ChIP-seq libraries, which may be caused by differences in washing conditions and/or differences in cell numbers used for the experiments. We also similarly analyzed the H3K27me3 data. Our results indicate that while about 38% to 53% of H3K27me3 reads from the ENCODE bulk cell H3K27me3 ChIP-seq libraries fell into the DHS regions (**Supplemental Table S5B**), about 33% to 41% of the H3K27me3 reads from the pooled single cells fell into the DHS regions. Thus the percentage of the H3K27me3 reads from the iscChIC-seq libraries in DHS regions is slightly lower than that from the bulk cell libraries, indicating that the H3K27me3 reads detected by iscChIC-seq are not substantially biased toward open chromatin regions. To test if the iscChIC-seq reads are depleted

37 from heterochromatic regions, we compared the overlap of the H3K27me3 iscChIC-seq reads or ENCODE
38 Bulk cell H3K27me3 ChIP-seq reads with the ENCODE H3K9me3 ChIP-seq peaks. We found that a quarter of
39 them are overlapping with H3K9me3 peaks. (**Supplemental Fig. S11**). The similar percentage between
40 H3K27me3 iscChIC-seq data and ENCODE H3K27me3 bulk cell ChIP-seq data suggested that the iscChIC-seq
41 reads are depleted from heterochromatic regions. To further estimate the true positive and false positive rates of
42 the iscChIC-seq reads, we assumed that the peaks from pooled single cells that overlap with those from
43 ENCODE data are true positives while the peaks not overlapping with the ENCODE peaks are false positives.
44 The analysis revealed that while the false positive rate ranges from 1.6 to 2.0%, the true positive rate is about
45 27% to 22% for H3K4me3 and H3K27me3, respectively (**Supplemental Table S5C**). For scCUT&Tag(Kaya-
46 Okur et al. 2019), the false positive rate ranges from 11 to 7%, the true positive rate is about 44% to 51% for
47 H3K4me2 and H3K27me3, respectively. For scChIP-seq(Grosselin et al. 2019), the false positive rate ranges
48 from 14 to 28%, the true positive rate is about 77% to 57% for H3K4me3 and H3K27me3, respectively. While
49 iscChIC-seq has a lower true positive rate compared to other methods, it has also much lower false positive rate.
50

51 Since the same WBC populations were used in profiling single cell H3K4me3 and single cell H3K27me3, it
52 would be important to examine if a cluster annotated with a cell type from H3K4me3 iscChIC-seq data is
53 specifically correlated with the cluster annotated with the same cell type from H3K27me3 iscChIC-seq data.
54 H3K4me3, an active modification, and H3K27me3, a repressive modification, are co-localized at some key
55 regulatory genomic regions due to either bivalent modifications or cellular heterogeneity (Bernstein et al. 2006;
56 Roh et al. 2006; Wang et al. 2009; Wei et al. 2009). The relative levels of these two modifications at these
57 regions are related to each other and influence the expression of underlying genes(Roh et al. 2006). To test this
58 possibility, we first identified 7,873 TSS regions (+/- 2.5kb) which exhibited overlapping H3K4me3 and
59 H3K27me3 peaks from the bulk cell H3K4me3 and H3K27me3 ChIP-seq data in monocytes, T cells, B cells,
60 and NK cells. Next, we identified cluster-specific H3K4me3 peaks among the 7,873 bivalent genes from the
61 H3K4me3 iscChIC-seq data, which are peaks that have higher H3K4me3 methylation level in one cell cluster
62 compared to all other clusters. To relate the H3K4me3 modification with H3K27me3 modification in the
63 iscChIC-seq datasets, we reasoned that when H3K4me3 level becomes higher, the H3K27me3 level should
64 become lower. Thus, from the four cell clusters based on the H3K27me3 iscChIC-seq data, we identified the
65 cluster-specific peaks among the 7,873 bivalent genes, which are peaks that have lower H3K27me3 methylation
66 level in one cluster compared to all other clusters. Comparison between these two kinds of cluster-specific
67 peaks revealed that the specific peaks of a H3K4me3 cluster is significantly overlapped with the specific peaks
68 of the H3K27me3 cluster if they are annotated as the same cell type (**Fig. 5A**). These results indicate that the
69 H3K4me3 level is negatively correlated to the H3K27me3 level in the bivalent genes. Further, we observed that
70 cell-to-cell variation in H3K4me3 and H3K27me3 was positively correlated at bivalent domains in monocytes

71 **(Fig. 5B)**. To match the clusters from single cell H3K4me3 and H3K27me3 data, we repeated the correlation
72 analysis for B cells, NK cells and T cells. Therefore, clusters annotated as B, T, monocyte, and NK from
73 H3K4me3 data were compared with the clusters annotated as B, T, monocyte, and NK from H3K27me3 data.
74 By computing the correlation between the cell-to-cell variation in these clusters (**Methods**), we found that B, T,
75 monocyte, NK clusters from H3K4me3 data have the highest correlation with B, T, monocyte, NK clusters from
76 H3K27me3 data, respectively (**Fig. 5C**). The p-value of this observation is 4×10^{-4} (**Methods**). This result
77 suggests that cell-to-cell variations in H3K4me3 and H3K27me3 are potentially coregulated in the bivalent
78 domains, which can be used to correlate the cell clusters identified from H3K4me3 and H3K27me3 single cell
79 data.

30
31 In this study, we developed iscChIC-seq to profile histone modification marks in single cells. This technique
32 employs the highly efficient TdT enzyme combined with T4 DNA ligase to add a unique barcode to the DNA
33 ends generated by antibody-guided MNase cleavage in each cell. Overall, we conclude that iscChIC-seq is a
34 reliable method for studying histone modifications at the single cell level, which provide important information
35 for the differentiation status of cells.

36 37 38 **DISCUSSION**

39
40 H3K4me3 is usually associated with gene activation, while H3K27me3 is associated with gene repression. Our
41 previous single-cell H3K4me3 data indicated that the cell-to-cell variation in H3K4me3 is correlated with the
42 cell-to-cell variation in gene expression (Ku et al. 2019), suggesting that single-cell histone modification data is
43 useful in understanding the cellular heterogeneity in gene expression. However, due to the relatively small
44 number of single-cells (scChIC-seq assay) or relatively sparse unique reads (iACT-seq and scCUT&Tag), the
45 application of current techniques are limited. In this study, we combined the TdT+T4 DNA ligase-mediated
46 barcoding strategy with the scChIC-seq protocol for iscChIC-seq, which enabled the analysis of either active or
47 repressive histone modification profiles in more than 10,000 single cells in one experiment. The assay captured
48 11,000 unique reads for H3K4me3 or 45,000 reads for H3K27me3 per single cell, which are better than other
49 high throughput techniques for histone modifications. Different from PA-TN5-based techniques, iscChIC-seq
50 works well for both active and repressive marks. Comparison with the bulk cell ChIP-seq data indicated that
51 iscChIC-seq does not have substantial bias toward open chromatin regions for either active or repressive histone
52 modification marks. In addition, iscChIC-seq does not require expensive equipment or special reagents and thus
53 easily accessible to most laboratories with molecular biology capabilities. Since PA-MNase effectively cleaves
54 chromatin even in the presence of formaldehyde crosslinking, which stabilizes chromatin binding proteins, bulk

cell ChIC-seq is capable of detecting genome-wide binding sites of transcription factors and other chromatin proteins. Thus, although the specificity of iscChIC-seq appears to be comparable or slightly lower than PA-TN5 based methods for detecting histone modifications, it is potentially applicable to profiling transcription factors and chromatin modifying enzymes at a single cell level.

Our analysis in this study indicated that both the active H3K4me3 and repressive H3K27me3 iscChIC-seq data are effective in clustering the complex WBCs and sorting out different cell types. H3K4me3 and H3K27me3 are colocalized to a subset of genomic regions, which are termed “bivalent domains” (Bernstein et al. 2006; Roh et al. 2006). Bivalent modifications are usually associated with key differentiation regulator genes and thus show substantial changes during cell development or differentiation (Bernstein et al. 2006; Wei et al. 2009) and the expression of a bivalent gene is correlated with the relative level of H3K4me3 and H3K27me3 signals at the gene locus (Roh et al. 2006). Although the overlap of H3K4me3 and H3K27me3 peaks at these genomic regions may be caused by different mechanisms including true bivalent modifications and cellular heterogeneity, the dynamic equilibrium of the two opposing modifications at these regions result from the competition of the corresponding enzymes to these regions. Hence, the two functionally opposite modifications may be co-regulated but demonstrate opposite directions. Indeed, our data showed that the increased H3K4me3 levels in bivalent genes in one type of cell cluster are positively correlated with the decreased H3K27me3 levels in the same bivalent genes in the same type of cell cluster. The cell-to-cell variations in H3K4me3 and H3K27me3 are positively correlated and exhibit the highest correlation when the cell cluster annotated from the H3K4me3 iscChIC-seq data matches with the same type of cell cluster annotated from the H3K27me3 iscChIC-seq data. Thus, these properties of bivalent modifications can be used to specifically correlate the cell clusters annotated from different single cell H3K4me3 and H3K27me3 data.

Overall, our data show that iscChIC-seq is a reliable single-cell technique for measuring histone modifications and potentially for chromatin binding proteins, which may find broad applications in studying cellular heterogeneity and differentiation status in complex developmental and disease systems.

METHODS

iscChIC-seq method

Reagents

Histone H3 trimethyl Lys4 antibody were purchased from Millipore (catalog no. 07-473), histone H3 trimethyl Lys27 antibody were purchased from Diagenode (catalog no. pAb-069-050). Methanol-free formaldehyde

39 solution and DSG (disuccinimidyl glutarate) were purchased from Thermo Fisher Scientific (catalog no. 28906,
40 20593). Terminal Transferase was purchased from New England BioLabs (catalog no. M0315L).

41 42 **PA-MNase induction and purification**

43 PET15b-PA-MNase plasmid (Addgene#124883) was transformed into BL21 Gold (DE3) following standard
44 protocol and grow in 40 ml LB medium (containing Ampicillin) overnight. Culture was diluted (1:50) into
45 prewarmed LB medium (containing Ampicillin) and shake for 2 hours at 37°C till OD600 reached ~0.6. Fresh
46 IPTG was added to the culture to final 1mM and shake for another 2.5 hours. For PA-MNase purification, cells
47 pellet was collected, resuspended in 30ml lysis buffer (50mM NaH₂PO₄, 300mM NaCl, 10mM Imidazole, 1x
48 EDTA-free protease inhibitor cocktails, 0.5 mM PMSF) supplemented with 30mg Lysozyme (Thermo Fisher
49 Scientific) and incubated on ice for 30 min. Cell lysate was sonicated for 10 cycles (10 sec on, 10 sec off) and
50 centrifuged at 10,000g for 20 min. Sonicator Misonix 4000 is used for sonication. In the meantime, 2ml 50%
51 bead slurry were washed with lysis buffer. Then the supernatant was collected, mixed with beads slurry and
52 rotated at 4°C for 1h. After spinning down, the beads were washed 4 times with 8ml wash buffer (50mM
53 NaH₂PO₄, 300mM NaCl, 20mM Imidazole, 1× EDTA-free protease inhibitor cocktails, 0.5 mM PMSF),
54 followed by three times elution with elution buffer(50mM NaH₂PO₄, 300mM NaCl, 250mM Imidazole, 1×
55 EDTA-free protease inhibitor cocktails, 0.5 mM PMSF). The purified fraction was mixed with glycerol, finally
56 aliquoted into small tubes and stored in -80°C.

57 58 **WBC preparation**

59 Human blood samples were obtained from healthy donors from the NIH Blood Bank. The WBCs were isolated
60 as described(Ku et al. 2019). Two-step fixation was modified from(Tian et al. 2012) and performed at room
61 temperature. First, 50M cells were suspended in 50ml PBS/MgCl₂ containing 2mM DSG and rotated for 45
62 min. After washing with PBS, the cells were resuspended in 45ml culture medium DMEM containing 10%
63 FBS. 3ml 16% formaldehyde was added to 1% final concentration and rotated for 5 min, then the reaction was
64 stopped by adding glycine, followed by two times washes with PBS. The cells were aliquoted into 2×10⁶ cells
65 per tube, frozen on dry ice, and stored at -80°C until use.

66 67 **MNase digestion**

68 To prepare ProteinA-MNase and antibody complex, 10 µl antibody and 25 µl PA-MNase were pre-incubated on
69 ice in 40 µl antibody binding buffer (10 mM Tris-Cl (pH 7.5), 1 mM EDTA, 150 mM sodium chloride, 0.1%
70 Triton X-100) for 30 min. Meanwhile, the fixed cells (0.25 million) were thawed on ice and resuspended in 200
71 µl antibody binding buffer. For H3K27me3 analysis, chromatin need to be firstly decondensed by suspending

72 the fixed cells in 0.5ml RIPA buffer (10 mM Tris-Cl (pH 7.5), 1 mM EDTA, 150 mM sodium chloride, 0.2%
73 SDS, 0.1% sodium deoxycholate, 1% Triton X-100) and incubated at room temperature for 10min followed by
74 one time wash in 0.5ml antibody binding buffer. Then the cells were mixed with PA-MNase and antibody
75 complex, incubated on ice for 60 min, followed by three washes with 500 μ l high salt buffer (10 mM Tris-Cl
76 (pH 7.5), 1 mM EDTA, 400 mM sodium chloride and 1% (v/v) Triton X-100). After washing in 200 μ l rinsing
77 buffer (10 mM Tris pH7.5, 10 mM sodium chloride and 0.1% (v/v) Triton X-100), the cells were resuspended in
78 40 μ l reaction solution buffer (10 mM Tris-Cl (pH 7.4), 10 mM sodium chloride, 0.1% (v/v) Triton X-100, 2
79 mM CaCl₂) to activate MNase digestion and incubated at 37°C for 3min in water bath. The reaction was
80 stopped by adding 4.4 μ l 100mM EGTA. The cells were pelleted by centrifugation at 500g for 5min.

81 **TdT&T4 ligation**

82 The MNase cleavage sites were end-repaired by T4 Polynucleotide Kinase (PNK) for removal of 3'-phosphoryl
83 groups and addition of 5'-phosphates to allow subsequent poly(G) tailing and ligation. After digestion, the cells
84 were washed twice with 1ml 1 \times T4 ligase buffer containing 0.1% NP40, then suspended in 300 μ l mixed T4
85 PNK buffer (1 \times T4 PNK buffer, 1 mM ATP, 30 μ l T4 PNK enzyme) and incubated at 37°C for 30min.
86 Meanwhile, 96 barcode-P7 adaptors (**Supplemental Table S2**) were thawed, 2.5 μ l 10 μ M barcode-P7 adaptors
87 were added to a new 96 well PCR plate with multichannel pipette (1 barcode per well). After incubation, the
88 cells were washed once with 1ml rinsing buffer, suspended with 516 μ l nuclei re-suspension buffer (1.27 \times T4
89 ligase buffer, 2.5 mM dGTP, 0.05% NP40), and mixed with 526 μ l enzyme dilution buffer (1.25 \times T4 ligase
90 buffer, 52.5 μ l Terminal Transferase, 78 μ l T4 ligase). Then 10 μ l cell suspension was aliquoted, mixed with the
91 2.5 μ l barcode-P7 adaptor in each well. Finally, the 12.5 μ l reaction mixture (1 \times T4 ligase buffer, 1 mM dGTP,
92 0.02% NP40, 0.5 μ l Terminal Transferase, 0.75 μ l T4 ligase) in the 96 well PCR plate was sealed completely
93 and incubated at 37°C for 60min.

94 **Pool and split**

95 After barcoding the MNase cleavage sites, the reaction system in the 96 wells were pooled together in a solution
96 trough containing 500 μ l stop buffer (10mM Tris-HCl (pH 8.0), 150mM NaCl, 10mM EDTA, 0.1%(v/v) Triton
97 X-100), the cells were pelleted, resuspended in 800 μ l PBS and send to flow cytometry core. 30 cells were
98 sorted in each well of a new 96 well plate using a BD FACSAria III cell sorter (BD Biosciences) and collected
99 in 10 μ l PBS containing 0.1% NP40. Totally 5 plates were collected. After adding 3 μ l reverse-crosslink buffer
100 (50mM Tris-HCl (pH 8.0), 25ng/ml Proteinase K and 0.1%NP40) into each well by multichannel pipette, the
101 plates were sealed completely, incubated in PCR machine for 65 °C overnight and 80 °C 10min to inactivate
102 Proteinase K.

06 Library preparation and sequencing

07 After reverse-crosslink, the DNA fragments with barcode adaptors were captured and labeled with second
08 library indexes through 12 cycles of annealing and extension with 96 PCR1 index primers (**Supplemental**
09 **Table S2**). The reaction was carried out by adding 15 μ l 2 \times Phusion[®] High-Fidelity PCR Master Mix with HF
10 Buffer (New England BioLabs) and 2.5 μ l 2 μ M index primer (1 index per well) into the reverse-crosslinked
11 solution in 96 wells. Then all the libraries were pooled together as described above, digested with 96 μ l
12 Exonuclease I (Thermo Fisher Scientific) at 37°C for 30min to degrade the excess index primers. The DNAs
13 were purified by MinElute[®] Reaction Cleanup Kit (Qiagen) and eluted with 64 μ l EB buffer (Qiagen). The A
14 tailing was performed in 1 \times NEBuffer 2 (New England BioLabs) by adding the Klenow fragment (3'→5' exo-)
15 (New England Biolabs) and 1 mM deoxyATP (New England Biolabs). After incubation at 37°C for 30 min, the
16 DNAs were purified and eluted by 23 μ l EB buffer. Then the Illumine P5 adaptor was ligated to the A-tailing
17 fragments using the T4 DNA ligase (New England BioLabs) by incubation at 16°C overnight. The DNAs were
18 purified again and eluted by 15 μ l EB buffer. PCR2 amplification was performed by adding the Phusion[®] High-
19 Fidelity PCR Master Mix with HF Buffer, i5 index primer (**Supplemental Table S2**) and P7-cs2 primer
20 (**Supplemental Table S2**) in the following condition: 98 °C 3 min, 57 °C 3 min, 72 °C 1 min, 15 cycles of 98
21 °C 10s, 65 °C 15s, 72 °C 30s, followed by 72 °C 5 min. Then the PCR products were run on the 2% E-Gel[®] EX
22 Agarose Gel (Invitrogen), the 250–600 base pair (bp) fragments were isolated and purified using the MinElute
23 Gel Extraction Kit (Qiagen). The concentration of the library was measured by Qubit dsDNA HS kit (Thermo
24 Fisher Scientific). The paired-end sequencing was performed on Illumina HiSeq 3000.

26 **Data analysis**

28 Demultiplexing and data analysis of *iscChIC*-seq libraries

29 The scripts for de-multiplexing and genome-wide mapping are available at
30 <https://github.com/wailimku/iscChIC-seq.git>. For profiling each type of histone marks, 30 single cells were
31 sorted into each of the 480 wells by FACS and sent to sequencing after the library's preparation steps. All
32 sequencing data was paired-end. The R2 reads contained the information of cell barcodes (**Supplemental Table**
33 **S2**), in which the cell barcode sequences followed the common sequence
34 AGAACCATGTCGTCAGTGTCCCCCCCC. For each well, R1 reads were mapped to the human reference
35 genome (UCSC hg18) using Bowtie2 (Langmead and Salzberg 2012). Using the cell barcode information from
36 R2 reads, we separated the mapped R1 reads into 96 sets corresponding to the 96 cell barcodes. Reads with
37 mapping quality less than 10 were removed. To remove duplicated reads, for each barcode, all the identical
38 reads were set as one read. Note that hg18 was used in this study because the current study is a follow-up study
39 of scChIC-seq (where hg18 was used). Thus, a direct comparison between the data sets could be performed. We

10 have mapped the reads of some samples to both hg18 and hg19 and observed that their mappability and
11 genome-wide profiles are highly similar. Thus, we believe that the use of hg18 in this study would not affect the
12 conclusions.

13
14 The estimated number of single cells in each well is based on the calculation strategy in the previous study
15 (Rubin et al. 2019). In our iscChIC-seq experiment, the cells were distributed into 96 wells such that each well
16 received 30 cells. Therefore, the number of barcodes predicted to not represent any cells = $96(1 - 1/96)^{30} =$
17 70.12. There are at least 25 (=96-70.12) barcodes representing cells. We assumed that the top-ranked barcodes
18 based on the number of reads correspond to cells. Similar to the previous study (Rubin et al. 2019), we used a
19 conservative cutoff of 1,000 reads per cell. As a result, combining all single cell data from the 480 wells, we
20 identified about 10,000 single cells for both H3K4me3 and H3K27me3. The mapping statistics for each of the
21 single cells were included in **Supplemental Table S3**.

22 ***Quality analysis of the single cell data***

23 ***Visualization in Genome Browser.*** For H3K4me3 and H3K27me3, 2,000 single cells were randomly selected
24 (matlab command: randperm (N, 2000)) and pooled together as the pseudo-bulk cell data. This pseudo-bulk cell
25 data was visualized using the WashU genome browser (Zhou et al. 2011) (**Figs. 2A and 4A**). For H3K4me3, to
26 compare with a benchmark, the H3K4me3 ChIP-seq data of different human white blood cells types (see
27 **Supplemental Table S4**) was downloaded from the ENCODE (Kazachenka et al. 2018) project shown in the
28 genome browser (**Fig. 2A**). For H3K27me3, to compare with a benchmark, we also downloaded the H3K27me3
29 ChIP-seq data of different human white blood cells types (see **Supplemental Table S4**) from the ENCODE
30 Project and visualized in the genome browser (**Fig. 4A**).

31
32 ***Peaks calling.*** To examine the quality of the single cell data, we compared the pooled single cell data to the
33 bulk cell ChIP-seq data downloaded from ENCODE (Kazachenka et al. 2018). For both H3K4me3 and
34 H3K27me3 marks, the information of the ENCODE data used in comparison could be found in **Supplemental**
35 **Table S4**. Peaks of this ENCODE data were called using SICER (Zang et al. 2009; Xu et al. 2014). A final set
36 of peaks for each histone marks was obtained by combining the peaks from different immune cell types.
37 Totally, the final combined sets of peaks obtained from ENCODE data contained 52,798 and 79,100 peaks for
38 H3K4me3 and H3K27me3, respectively. Peaks from the pooled single cells were identified using SICER and
39 their widths were fixed to be 3,000 and 10,000 for H3K4me3 and H3K27me3, respectively. The overlap
40 between peaks from the pooled single cells and the bulk-cell data were computed using the BEDTools (Quinlan
41 and Hall 2010) intersect commands “BEDTools intersect -wa -a the pooled peak file -b the bulk cell peak file
42

73 **(Supplemental Fig. S12)**. Therefore, the criteria of overlapped peaks from pooled cell and bulk cell data that
74 there is at least 1bp overlap.

75
76 *Scatter plots.* The human genome was equally divided into bins (bin size = 5kb for H3K4me3; bin size = 50kb
77 for H3K27me3). The 50kb bin size was selected as in a previous study (Grosselin et al. 2019), because
78 H3K27me3 peaks spanned broad regions. For both bulk cell and pooled single cell libraries, the read density
79 (counts per million, CPM) at each bin was calculated. The correlation between the logarithm of the read
80 densities of two libraries was quantified using the Pearson's correlation coefficient (**Figs. 2C and 4C**).

81
82 *TSS profile plots.* For H3K4me3, the software Homer(Heinz et al. 2010) was used to calculate the TSS density
83 profile (annotatePeaks.pl tss hg18 -size 3000 -hist 20 -len 1) for each single cells. In particular, a region of 3kb
84 around each TSS was considered. This region was then divided into 150 bins. The density profile was generated
85 using the number of reads mapped onto the bin divided by the total number of mapped reads and averaged over
86 all promoters.

87 *Estimate of the collision rate in Human and mouse mixing experiments*

88
89 The same procedure of identification of cells were used for the species mixing data set. Reads were mapped to
90 both hg18 and mm9 reference genome using Bowtie2. Cells were identified using the procedure described
91 above, in which the top-ranked barcodes based on the number of reads correspond to cells. We also used the
92 same cutoff of 1,000 reads per cell. We identified human and mouse collision as those that had less than a 15×
93 enrichment over the minor genome. The collision rate is estimated as two times the number of human and
94 mouse collision over the total number of cells. Note that we have mapped the reads of some samples to both
95 mm9 and mm10 and observed that their mappability and genome-wide profiles are highly similar. Thus, we
96 believe that the use of mm9 in this study would not affect the conclusions.

97 *Clustering analysis for the iscChIC-seq data*

98
99 *Expression matrix.* Single cells with reads more than 3,000 (4,000) were first selected. This resulted in 7798 and
100 9207 single cells for H3K4me3 and H3K27me3, respectively. Second, it was required that the fraction of reads
101 in peaks higher than 0.15 (0.15) were selected for clustering analysis for H3K4me3 (H3K27me3) single cell
102 data. This resulted in 6,021 and 7,038 single cells for H3K4me3 and H3K27me3, respectively.

103
104 For each cell in H3K4me3 (H3K27me3), reads located within the 52,978 (79,100) combined H3K4me3
105 (H3K27me3) were counted. We applied a consensus clustering approach, that is similar to SC3(Kiselev et al.
106 2017), to the iscChIC-seq data. First, we computed a read count matrix **R**, in which the columns correspond to

77 cells and rows correspond to the peaks. R_{ij} indicates the number of reads at the i th peak from the j th cell. Each
 78 column in the read count matrix was divided by the library size and multiplied by a factor of 10^6 . The resulting
 79 matrix denoted as \mathbf{M} . The \log_2 transformation was further applied resulting \mathbf{M}' where $\mathbf{M}' = \log_2(\mathbf{M} + 1)$. For
 80 filtering the non-informative bins, a binary matrix \mathbf{M}^b was obtained from \mathbf{M}' and defined as,

$$M^b_{ij} = \begin{cases} 0, & \text{if } M'_{ij} \leq 0, \\ 1, & \text{if } M'_{ij} > 0. \end{cases}$$

81 The i th row (peak) in the matrix \mathbf{M}' would be selected if $\sum_{j=1}^{\text{total \# of cell}} M^b_{ij} < C_{peak}$, where C_{peak} is a cutoff
 82 value equal to 100 for both H3K4me3 and H3K27me3, respectively. The filtering of these bins is based on the
 83 assumption that reads at a bin should be found in more single cells if the bin is more informative. We denoted
 84 the expression matrix after the deletion of rows (peaks) as \mathbf{M}'' .

85
 86 Calculation of the Laplacian matrix. Consider \mathbf{m}_j to be a vector equal to the j th column (cells) of \mathbf{M}'' . First, we
 87 computed the similarity between cells using the Pearson's correlation, and resulting a correlation matrix \mathbf{C} . In
 88 particular, C_{ij} is the Pearson's correlation value between the vectors \mathbf{m}_j and \mathbf{m}_i . Thus, the rows and columns of
 89 the matrix \mathbf{C} correspond to single cells. The Laplacian matrix \mathbf{L} is defined by $\mathbf{L} = \mathbf{I} - \mathbf{D}^{-1/2}\mathbf{A}\mathbf{D}^{-1/2}$, where \mathbf{I} is
 90 the identity matrix. \mathbf{A} is a similarity matrix where $\mathbf{A} = e^{-(2-\mathbf{C})/\max(2-\mathbf{C})}$. Note that \mathbf{D} is the degree matrix of \mathbf{A} ,
 91 a diagonal matrix that contains the row-sums of \mathbf{A} on the diagonal ($D_{ii} = \sum_i A_{ij}$). We computed the eigenvectors
 92 of the Laplacian matrix and formed a matrix \mathbf{V} where each column represents an eigenvector. The columns of \mathbf{V}
 93 from left to right are sorted in ascending order based on their corresponding eigenvalues.

94
 95 Optimal number of clusters. We applied the silhouette analysis to determine the optimal number of clusters.
 96 First, we created a matrix \mathbf{W}^{s_1} , which is a submatrix of \mathbf{V} and $W_{ij}^{s_1} = V_{ij}$. Note that i is from 1 to the total
 97 number of bins and $j=1, \dots, s_1$. s_1 is fixed to be 12 for both H3K4me3 and H3K27me3. Note that we have tried
 98 s_1 to be larger than 12 up to 20. We observed that the results are the same. Here we showed the results up to 12.
 99 We applied the k -means method to the matrix \mathbf{W}^{s_1} for clustering single cells into k clusters and computed the
 100 silhouette coefficient for the clusters. By varying the number of clusters k from 4 to 12, we determine the
 101 optimal k value by selecting the case of k having the largest silhouette coefficient value. The optimal k is equal
 102 to six for both H3K4me3 and H3K27me3.

103
 104 Clustering. A binary matrix \mathbf{E} was considered in which its rows and columns correspond to single cells. The k -
 105 means method was applied to the matrix \mathbf{W}^{s_1} to cluster the single cells with $k = 6$. If cells i and j belong to the
 106 same cluster, $E_{ij} = E_{ji} = 1$; otherwise 0. We consider s_1 is between 2 to 15 and. For each s_1 , we repeated the

37 clustering analysis for 10 times and thus obtaining 10 different E s. A final matrix E^c is calculated by averaging
 38 all binary matrices from each individual clustering.

39
 40 *t-SNE visualization.* We applied the dimension reduction method t-SNE to the matrix E^c . The position of single
 41 cells is visualized in the two-dimensional t-SNE representative space. Note that t-SNE was used for
 42 visualization while cells were clustered by applying *k-means* method to E^c .

43
 44 *Hypergeometric test.* A hypergeometric-based test was used to assess the significance of peaks that are both
 45 cluster specific and cell type specific. The rationale behind using the hypergeometric test was that if a cluster
 46 specific peak had any biological and/or functional association to a cell type, they would also be cell type
 47 specific in a higher number of samples than expected by chance. We tested the null hypothesis that the property
 48 for a peak that are cluster specific and that are cell type-specific are independent.

51 *Clusters annotation for both H3K4me3 and H3K27me3*

52 *Cluster annotations.* After clustering single cells from the single cell H3K4me3 or H3K27me3 data, we
 53 annotated the clusters to cell types using the bulk cell ENCODE data. First, we downloaded the H3K4me3 and
 54 H3K27me3 ENCODE data for B cells, monocytes, T cells, and NK cells. There were at least two replicates for
 55 each histone marks and each cell type. For both H3K4me3 and H3K27me3, the density matrices with \log_2
 56 transformation ($V^B, V^{mono}, V^T, V^{NK}$), which was similar to M'' , were computed for the four cell types,
 57 respectively. The number of rows was equal to the number of peaks while the number of columns was equal to
 58 the number of replicates. Note that the peaks in ($V^B, V^{mono}, V^T, V^{NK}$) were the same as those in M'' . The two-
 59 sided student's *t*-test was used to compute the cell type-specific peaks from the four density matrices
 60 ($V^B, V^{mono}, V^T, V^{NK}$). The *i*th row vector of the matrix V^Z ($Z = B, mono, T, or NK$) was denoted as v_i^Z . The
 61 *i*th peak (row) was specific to a cell type Z if v_i^Z is significantly higher than all v_i^Y with a p-value of 0.05 **and**
 62 $mean(v_i^Z) - mean(v_i^Y) > a\ cutoff$ (0.4 for H3K27me3, and 0.2 for H3K4me3), where
 63 $Y = B, mono, T, NK$ and $Y \neq Z$. Different cutoff values were selected because we assumed that the bulk cell
 64 and the pooled single cells should give similar number of peaks. For the purpose of cluster annotation, the sets
 65 of cell type-specific peaks (specific to cell type Z) were denoted as $S_{4,an,Z}$ and $S_{27,an,Z}$ for the H3K4me3 and
 66 H3K27me3 bulk cell data, respectively. Note that the statistical significance of cell type-specific peaks and
 67 cluster-specific peaks were determined by P-value instead of FDR since very few cell type-specific peaks were
 68 discovered from ENCODE ChIP-seq data when using FDR.

70 For each histone mark, pseudo-bulk \log_2 density matrices ($W^1, W^2, W^3, W^4, W^5, W^6$) were computed for
 71 cluster 1, 2, 3, 4, 5, and 6, respectively. In each of these matrices, the number of columns was equal to the
 72 number of peaks while the number of rows was equal to the number of pseudo-bulk replicates. Note that the
 73 peaks in ($W^1, W^2, W^3, W^4, W^5, W^6$) were the same as those in M'' . To generate W^i ($i = 1, 2, 3, 4, 5, 6$), six
 74 sub-samples of cells were randomly selected from the cells belonging to cluster i , in which the size of each
 75 subsample was equal to one-third of the number of cells belonging to cluster i . By pooling the cells in each sub-
 76 sample, the \log_2 density for each peak was calculated for obtaining W^i . The j th row of W^i was denoted as w_j^i .
 77 The j th peak was specific to a cluster i if w_j^i was significantly higher than all w_j^k , where
 78 $k = 1, 2, 3, 4, 5, 6$ and $k \neq i$. Note that p-value computed by the two-sided student's t -test was required to be
 79 smaller than 0.05 and $mean(w_j^i) - mean(w_j^k)$ was higher than a *cutoff* (0.1 for both H3K4me3 and
 80 H3K27me3). The sets of cluster-specific peaks (specific to cluster i) for the use of cluster annotation were
 81 denoted as $X_{4,an,i}$ and $X_{27,an,i}$ for the H3K4me3 and H3K27me3 bulk cell data, respectively.

82
 83 The set of cluster-specific peaks and cell type-specific peaks were compared. For H3K4me3 data, the p-value
 84 for the intersect between a cell type Z and a cluster i ($X_{4,an,i} \cap S_{4,an,Z}$) was computed by the hypergeometric
 85 test. A cluster i was considered to be annotated validly to a cell type Z if the p-value for ($X_{4,an,i} \cap S_{4,an,Z}$) is
 86 smaller than 1×10^{-5} and the p-value for other comparisons ($X_{4,an,i} \cap S_{4,an,Y}, Y = B, mono, T, NK$ but $\neq Z$)
 87 is greater than 1×10^{-5} .

88
 89 Reproducibility of cluster annotations. To check how reproducible the cluster annotations is, we repeated the
 90 computations for 100 times and the cluster density matrices were re-generated each time via the same sub-
 91 sampling procedures. The mean and the standard deviation of the p-value in the comparisons were computed
 92 and shown in **Figs 3B** and **4E**. Also, the frequency for a cluster to obtain a valid annotation was recorded and
 93 shown in **Supplemental Figs. 2B** and **2D**. To consider a cluster annotation is valid finally, we required that the
 94 frequency for a cluster to obtaining a valid annotation is greater than 0.9.

95
 96 Matching the clusters between H3K4me3 and H3K27me3 marks. For either single cell H3K4me3 or H3K27me3
 97 data, six clusters were found where four of them were annotated as monocytes s T cells, B cells, and NK cells,
 98 respectively. If a cluster obtained from single cell H3K4me3 data annotated with a cell type, this cluster was
 99 expected to correlate with the cluster obtained from single cell H3K27me3 data annotated with the same cell
 100 type.

02 Bivalent domains were defined as regions where H3K4me3 and H3K27me3 peaks obtained from ENCODE
 03 data that were overlapped (command: BEDTools intersect -a 'H3K27me3 peak file' -b 'H3K4me3 peak file';
 04 **Supplemental Fig. S12**), and required to be at least 100bp overlap for the estimation of one nucleosome
 05 overlap. 25,951 bivalent domains were obtained, in which 7,989 bivalent domains were overlapped with the
 06 TSS regions. For both single cell H3K4me3 and H3K27me3 data, we computed the pseudo-bulk log₂ density
 07 matrices ($W^{B,4}, W^{mono,4}, W^{T,4}, W^{NK,4}$ and $W^{B,27}, W^{mono,27}, W^{T,27}, W^{NK,27}$) for clusters annotated to B
 08 cells, Monocytes, T cells and NK cells, respectively. To generate $W^{Z,4}$ or $W^{Z,27}$, six sub-samples of cells were
 09 randomly selected from the cells belonging to cluster annotated to cell type Z , in which the size of each
 10 subsample was equal to two-third of the number of cells belonging to that cluster. By pooling the cells in each
 11 sub-sample, the log₂ density for each peak was calculated for obtaining $W^{Z,4}$ or $W^{Z,27}$. The j th row of $W^{Z,4}$
 12 was denoted as $w_j^{Z,4}$ while the j th row of $W^{Z,27}$ was denoted as $w_j^{Z,27}$. A peak was specific to a H3K4me3
 13 cluster annotated to cell type Z if $w_j^{Z,4}$ was significantly higher than all $w_j^{Y,4}$ where $Y = B, mono, T, NK$ but $Y \neq$
 14 Z . Note that FDR of the p-value (computed by the two-sided student's t -test) was required to be smaller than
 15 0.05 and $mean(w_j^{Z,4}) - mean(w_j^{Y,4})$ was larger than 0.3. A peak was specific to a H3K27me3 cluster
 16 annotated to cell type Z if $w_j^{Z,27}$ was significantly lower than all $w_j^{Y,27}$ where $Y = B, mono, T, NK$ but $Y \neq$
 17 Z . Note that FDR for the p-value was required to be smaller than 0.05 and
 18 $mean(w_j^{Z,27}) - mean(w_j^{Y,27})$ was smaller than 0.3. The sets of cluster-specific peaks (specific to cluster
 19 annotated to cell type Z) for the use of matching H3K4me3 and H3k27me3 clusters were denoted as $X_{4,mat,Z}$
 20 and $X_{27,mat,Z}$ for the H3K4me3 and H3K27me3 clusters, respectively. The p-value for the intersection
 21 $X_{4,mat,Z} \cap X_{27,mat,Y}$ was computed by hypergeometric test, where $Z, Y = B, mono, T, NK$.
 22
 23

24 Relationship between cell-to-cell variation in H3K4me3 and H3K27me3. Different from the procedures of
 25 matching the H3K4me3 and H3K27me3 clusters, all bivalent domains were considered. Also, instead of
 26 calculating the pseudo-bulk log₂ density matrices, the vectors of coefficients of variation ($cv^{B,4}, cv^{mono,4},$
 27 $cv^{T,4}, cv^{NK,4}$ and $cv^{B,27}, cv^{mono,27}, cv^{T,27}, cv^{NK,27}$) were calculated for the H3K4me3 and H3K27me3
 28 clusters annotated to B cells, Monocytes, T cells and NK cells, respectively. Similar to the single cell log₂
 29 density matrices M'' , the log₂ density matrices for single cells in H3K4me3 and H3K27me3 clusters were
 30 denoted as ($M^{B,4}, M^{mono,4}, M^{T,4}, M^{NK,4}, M^{B,27}, M^{mono,27}, M^{T,27}$ and $M^{NK,27}$) referring to H3K4me3 and
 31 H3K27me3 clusters annotated to B cells, Monocytes, T cells and NK cells, respectively. Each of these density
 32 matrices has the dimensions of the number of bivalent domains multiplied by the number of single cells in the
 33 clusters. The vectors of coefficients of variation were computed using these density matrices over the single

34 cells. For the purpose of finding the relationship between *cell-to-cell variation in H3K4me3 and H3K27me3*, the
 35 j th bivalent domain was specific to a H3K4me3 cluster annotated to cell type Z if $\log_2 cv_j^{Z,4}$ is larger than all
 36 $\log_2 cv_j^{Y,4}$ than a cutoff (0.2) where $Y = B, mono, T, NK$ and $Y \neq Z$, and the number of non-zero elements in
 37 j th row of $M^{Z,4} M^{B,4}$ is larger than 5% of the mean of the number of non-zero elements overall all rows in
 38 $M^{Z,4}$. The second requirement is to only include those relatively more confident CV value for each cluster.
 39 The same calculation was applied to obtain the bivalent domains that were specific to a H3K27me3 cluster
 40 annotated to cell type Z . The sets of cluster-specific peaks (specific to cluster annotated to cell type Z) for the
 41 use of finding the relationship between cell-to-cell variation in H3K4me3 and H3k27me3 were denoted as
 42 $X_{4,CV,Z}$ and $X_{27,CV,Z}$ for the H3K4me3 and H3K27me3 clusters, respectively. By considering the bivalent
 43 domains in the set of $X_{4,CV,Z} \cap X_{27,CV,Y}$, the Spearman's correlation between $cv^{Z,4}$ and $cv^{Y,27}$ for and $Y, Z =$
 44 ***B, mono, T, and NK.***

46 **DATA access**

47 All raw and processed sequencing data generated in this study have been submitted to the NCBI Gene
 48 Expression Omnibus (GEO; <https://www.ncbi.nlm.nih.gov/geo/>) under accession number GSE139857.

50 **Software availability**

51 The code can be found in supplemental_code.zip or downloaded from [https://github.com/wailimku/iscChIC-](https://github.com/wailimku/iscChIC-seq.git)
 52 [seq.git](https://github.com/wailimku/iscChIC-seq.git).

54 **ACKNOWLEDGEMENTS**

55 We thank the National Heart, Lung, and Blood Institute DNA Sequencing Core Facility for sequencing the
 56 libraries; and the National Heart, Lung, and Blood Institute Flow Cytometry Core facility for sorting the cells.
 57 The work was supported by Division of Intramural Research, National Heart, Lung and Blood Institute.

59 **AUTHOR CONTRIBUTIONS**

60 K.Z. conceived the project. L.P. performed the experiments. W.L.K. analyzed the data. Y.C. contributed to data
 61 analysis. W.G. contributed to the design of the experiments. W.L.K., L.P. and K.Z. wrote the paper.

63 **COMPETING INTERESTS**

64 The authors declare that there are no competing interests.

66 **REFERENCES**

57

- 58 Ai S, Xiong H, Li CC, Luo Y, Shi Q, Liu Y, Yu X, Li C, He A. 2019. Profiling chromatin states using single-cell itChIP-
59 seq. *Nat Cell Biol* **21**: 1164-1172.
- 70 Barski A, Cuddapah S, Cui K, Roh TY, Schones DE, Wang Z, Wei G, Chepelev I, Zhao K. 2007. High-resolution
71 profiling of histone methylations in the human genome. *Cell* **129**: 823-837.
- 72 Bernstein BE, Mikkelsen TS, Xie X, Kamal M, Huebert DJ, Cuff J, Fry B, Meissner A, Wernig M, Plath K et al.
73 2006. A bivalent chromatin structure marks key developmental genes in embryonic stem cells. *Cell* **125**:
74 315-326.
- 75 Carter B, Ku WL, Kang JY, Hu G, Perrie J, Tang Q, Zhao K. 2019. Mapping histone modifications in low cell
76 number and single cells using antibody-guided chromatin tagmentation (ACT-seq). *Nat Commun* **10**:
77 3747.
- 78 Creighton MP, Cheng AW, Welstead GG, Kooistra T, Carey BW, Steine EJ, Hanna J, Lodato MA, Frampton GM,
79 Sharp PA et al. 2010. Histone H3K27ac separates active from poised enhancers and predicts
80 developmental state. *Proc Natl Acad Sci U S A* **107**: 21931-21936.
- 81 Cusanovich DA, Daza R, Adey A, Pliner HA, Christiansen L, Gunderson KL, Steemers FJ, Trapnell C, Shendure J.
82 2015. Multiplex single cell profiling of chromatin accessibility by combinatorial cellular indexing.
83 *Science* **348**: 910-914.
- 84 Gosselin K, Durand A, Marsolier J, Poitou A, Marangoni E, Nemati F, Dahmani A, Lameiras S, Reyat F, Frenoy O
85 et al. 2019. High-throughput single-cell ChIP-seq identifies heterogeneity of chromatin states in breast
86 cancer. *Nat Genet* **51**: 1060-1066.
- 87 Hainer SJ, Boskovic A, McCannell KN, Rando OJ, Fazio TG. 2019. Profiling of Pluripotency Factors in Single Cells
88 and Early Embryos. *Cell* doi:10.1016/j.cell.2019.03.014.
- 89 Harada A, Maehara K, Handa T, Arimura Y, Nogami J, Hayashi-Takanaka Y, Shirahige K, Kurumizaka H, Kimura
90 H, Ohkawa Y. 2019. A chromatin integration labelling method enables epigenomic profiling with lower
91 input. *Nat Cell Biol* **21**: 287-296.
- 92 Heinz S, Benner C, Spann N, Bertolino E, Lin YC, Laslo P, Cheng JX, Murre C, Singh H, Glass CK. 2010. Simple
93 combinations of lineage-determining transcription factors prime cis-regulatory elements required for
94 macrophage and B cell identities. *Mol Cell* **38**: 576-589.
- 95 Johnson DS, Mortazavi A, Myers RM, Wold B. 2007. Genome-wide mapping of in vivo protein-DNA
96 interactions. *Science* **316**: 1497-1502.
- 97 Kaya-Okur HS, Wu SJ, Codomo CA, Pledgers ES, Bryson TD, Henikoff JG, Ahmad K, Henikoff S. 2019. CUT&Tag
98 for efficient epigenomic profiling of small samples and single cells. *Nature Communications* **10**.
- 99 Kazachenka A, Bertozzi TM, Sjoberg-Herrera MK, Walker N, Gardner J, Gunning R, Pahita E, Adams S, Adams D,
100 Ferguson-Smith AC. 2018. Identification, Characterization, and Heritability of Murine Metastable
101 Epialleles: Implications for Non-genetic Inheritance. *Cell* **175**: 1717.
- 102 Kim TH, Barrera LO, Zheng M, Qu C, Singer MA, Richmond TA, Wu Y, Green RD, Ren B. 2005. A high-resolution
103 map of active promoters in the human genome. *Nature* **436**: 876-880.
- 104 Kiselev VY, Kirschner K, Schaub MT, Andrews T, Yiu A, Chandra T, Natarajan KN, Reik W, Barahona M, Green AR
105 et al. 2017. SC3: consensus clustering of single-cell RNA-seq data. *Nat Methods* **14**: 483-486.
- 106 Ku WL, Nakamura K, Gao W, Cui K, Hu G, Tang Q, Ni B, Zhao K. 2019. Single-cell chromatin immunocleavage
107 sequencing (scChIC-seq) to profile histone modification. *Nat Methods* **16**: 323-325.
- 108 Langmead B, Salzberg SL. 2012. Fast gapped-read alignment with Bowtie 2. *Nat Methods* **9**: 357-359.
- 109 Mikkelsen TS, Ku M, Jaffe DB, Issac B, Lieberman E, Giannoukos G, Alvarez P, Brockman W, Kim TK, Koche RP et
110 al. 2007. Genome-wide maps of chromatin state in pluripotent and lineage-committed cells. *Nature*
111 **448**: 553-560.
- 112 Quinlan AR, Hall IM. 2010. BEDTools: a flexible suite of utilities for comparing genomic features. *Bioinformatics*
113 **26**: 841-842.

- 14 Robertson G, Hirst M, Bainbridge M, Bilenky M, Zhao YJ, Zeng T, Euskirchen G, Bernier B, Varhol R, Delaney A
 15 et al. 2007. Genome-wide profiles of STAT1 DNA association using chromatin immunoprecipitation and
 16 massively parallel sequencing. *Nature Methods* **4**: 651-657.
- 17 Roh TY, Cuddapah S, Cui K, Zhao K. 2006. The genomic landscape of histone modifications in human T cells.
 18 *Proc Natl Acad Sci U S A* **103**: 15782-15787.
- 19 Rotem A, Ram O, Shores N, Sperling RA, Goren A, Weitz DA, Bernstein BE. 2015. Single-cell ChIP-seq reveals
 20 cell subpopulations defined by chromatin state. *Nat Biotechnol* **33**: 1165-1172.
- 21 Rousseeuw PJ. 1987. Silhouettes - a Graphical Aid to the Interpretation and Validation of Cluster-Analysis. *J*
 22 *Comput Appl Math* **20**: 53-65.
- 23 Rubin AJ, Parker KR, Satpathy AT, Qi Y, Wu B, Ong AJ, Mumbach MR, Ji AL, Kim DS, Cho SW et al. 2019.
 24 Coupled Single-Cell CRISPR Screening and Epigenomic Profiling Reveals Causal Gene Regulatory
 25 Networks. *Cell* **176**: 361-376 e317.
- 26 Schmid M, Durussel T, Laemmli UK. 2004. ChIC and ChEC; genomic mapping of chromatin proteins. *Mol Cell*
 27 **16**: 147-157.
- 28 Tian B, Yang J, Brasier AR. 2012. Two-step cross-linking for analysis of protein–chromatin interactions. In
 29 *Transcriptional Regulation*, pp. 105-120. Springer.
- 30 Wang Q, Xiong H, Ai S, Yu X, Liu Y, Zhang J, He A. 2019. CoBATCH for High-Throughput Single-Cell Epigenomic
 31 Profiling. *Mol Cell* **76**: 206-216 e207.
- 32 Wang Z, Schones DE, Zhao K. 2009. Characterization of human epigenomes. *Curr Opin Genet Dev* **19**: 127-134.
- 33 Wei G, Wei L, Zhu J, Zang C, Hu-Li J, Yao Z, Cui K, Kanno Y, Roh TY, Watford WT et al. 2009. Global mapping of
 34 H3K4me3 and H3K27me3 reveals specificity and plasticity in lineage fate determination of
 35 differentiating CD4+ T cells. *Immunity* **30**: 155-167.
- 36 Xu S, Grullon S, Ge K, Peng W. 2014. Spatial clustering for identification of ChIP-enriched regions (SICER) to
 37 map regions of histone methylation patterns in embryonic stem cells. *Methods Mol Biol* **1150**: 97-111.
- 38 Zang C, Schones DE, Zeng C, Cui K, Zhao K, Peng W. 2009. A clustering approach for identification of enriched
 39 domains from histone modification ChIP-Seq data. *Bioinformatics* **25**: 1952-1958.
- 40 Zhou X, Maricque B, Xie M, Li D, Sundaram V, Martin EA, Koebe BC, Nielsen C, Hirst M, Farnham P et al. 2011.
 41 The Human Epigenome Browser at Washington University. *Nat Methods* **8**: 989-990.
- 42
 43
 44

45 Figure Legends

46

47 Figure 1. Schematic of iscChIC-seq

- 48 A. Experimental flow. (1) Bulk cells were split into the first 96 well plate after antibody guided MNase
 49 cleavage and end repair. (2) Barcoded cells were pooled together and sorted into the second 96 well
 50 plate to introduce i7 index. (3) Cells were pooled together again from each plate and labelled with i5
 51 index in PCR2.
- 52 B. Illustration of poly(dG) addition to DNA ends by TdT, oligo dC adaptor ligation by T4 DNA ligase,
 53 and PCR-mediated barcoding process. Cell barcode (red) is designed into the oligo dC P7 adaptor in
 54 which 3' ends are blocked to prevent non-template tailing by TdT. After reverse crosslinking,
 55 barcoded DNA fragments could be efficiently labeled with i7 index (purple) through annealing and

56 PCR extension. The barcoded P5 adaptor is added to the other end of genomic DNA fragments by
 57 ligation and PCR2, which is used to amplify the library DNA for NGS sequencing.

58
 59
 60 **Figure 2.** iscChIC-seq robustly detects H3K4me3 profiles in human white blood cells.

- 61 A. A genome browser snapshot showing panels of H3K4me3 profiles in human white blood cells. The
 62 top blue track shows the pooled single cell data from iscChIC-seq. The bottom track shows 500
 63 randomly selected single cells. The middle tracks display the ENCODE bulk cell ChIP-seq data from
 64 different cells indicated on the left.
- 65 B. A Venn diagram showing the overlap of the enriched regions (peaks) of H3K4me3 profiles
 66 measured by ChIP-seq using bulk cells and by the pooled single cell data.
- 67 C. A scatter plot of the H3K4me3 read density of ChIP-seq (bulk cell) versus that of pooled single cells
 68 from iscChIC-seq (2,000 cells were randomly selected) at the genome-wide divided bins (the size of
 69 bin is 5kb). The Pearson's correlation is equal to 0.89.
- 70 D. A TSS profile plot showing the H3K4me3 profile around TSS for all single cells (grey) and the
 71 pooled single cells (red).

72
 73 **Figure 3.** Identification of sub-cell types in white blood cells based on clusters generated from single-cell
 74 H3K4me3 profiles

- 75 A. A t-SNE visualization of cells by applying the t-SNE analysis on the matrix E^c . Cell type annotations
 76 of clusters are obtained by the analysis in **Fig. 3B**.
- 77 B. A heatmap showing the significance of the overlap between the cluster-specific peaks from the
 78 H3K4me3 iscChIC-seq data (**Fig. 3A**) and cell type-specific peaks from ENCODE H3K4me3 ChIP-
 79 seq data. The Y-axis refers to the cluster-specific peaks and X-axis refer to the cell type-specific
 80 peaks. The values before the +/- sign refer to the average negative logarithm of the P-value for the
 81 overlap between the two types of peaks over 100 subsamples. The values behind the +/- sign refer to
 82 the standard deviation of the negative logarithm of the P-value over 100 sub samples.
- 83 C. Genome browser snapshots showing the H3K4me3 profiles from bulk cells ChIP-seq data and pooled
 84 single-cell iscChIC-seq data. The ChIP-seq data for B cells, monocytes, T cells and, NK cells are
 85 downloaded from ENCODE (red). The pooled H3K4me3 iscChIC-seq data for each identified cell
 86 type (Fig. 3A) are displayed (blue). For the iscChIC-seq data, 1,610 monocytes, 1,265 T cells, 898
 87 NK cells, and 446 B cells were used.

38 D. A t-SNE visualization of cells by applying the t-SNE analysis on the matrix E^c . H3K4me3 density of
 39 regions associated with different genes is plotted. The color level indicates the H3K4me3 density
 40 level.

41
 42 **Figure 4.** iscChIC-seq robustly detects H3K27me3 profiles in human white blood cells

- 43
 44 A. A genome browser snapshot showing H3K27me3 profiles in human white blood cells. The top blue track
 45 shows the pooled single cell data from iscChIC-seq. The bottom track shows 500 randomly selected
 46 single cells. The middle tracks display the ENCODE bulk cell ChIP-seq data from different cells
 47 indicated on the left.
- 48 B. A Venn diagram showing the overlap of the enriched regions (peaks) of H3K27me3 profiles measured by
 49 ChIP-seq using bulk cells and by the pooled single cell data.
- 50 C. A scatter plot of the H3K27me3 read density of ChIP-seq (bulk cell) versus that of pooled single cells
 51 from iscChIC-seq (2,000 cells were randomly selected) at the genome-wide divided bins (the size of bin
 52 is 50kb). The Pearson's correlation is equal to 0.92.
- 53 D. A t-SNE visualization of cells by applying the t-SNE analysis on the matrix E^c . Cell type annotations of
 54 clusters are obtained by the analysis in **Fig. 4E**.
- 55 E. A heatmap showing the significance of the overlap between the cluster-specific peaks from the
 56 H3K27me3 iscChIC-seq data (**Fig. 4D**) and cell type-specific peaks from ENCODE H3K27me3 ChIP-
 57 seq data. The Y-axis refers to the cluster-specific peaks and X-axis refer to the cell type-specific peaks.
 58 The values before the +/- sign refer to the average negative logarithm of the P-value for the overlap
 59 between the two types of peaks over 100 subsamples. The values behind the +/- sign refer to the standard
 60 deviation of the negative logarithm of the P-value over 100 sub samples.

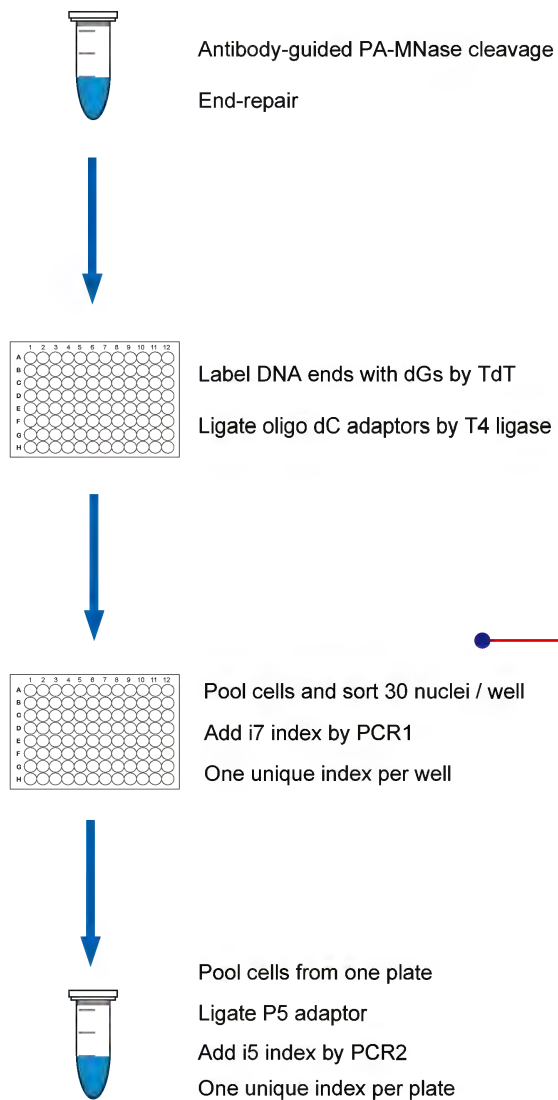
61
 62 **Figure 5.** Correlation of cell clusters revealed from the single cell H3K4me3 and H3K27me3 data by bivalent
 63 domains

- 64
 65 A. The cluster-specific peaks identified from the single-cell H3K4me3 and H3K27me3 data exhibit the
 66 highest overlap if they are from the same cell type. For each subplot, the cluster-specific peaks of
 67 H3K4me3 from one annotated cluster (as indicated on the top) were compared with the cluster-specific
 68 peaks of H3K27me3 from different clusters (as indicated below the plot). The Y-axis in each subplot
 69 indicates the $-\log_2$ of P-value for the overlap between the cluster-specific peaks of H3K4me3 and
 70 cluster-specific peaks of H3K27me3.

- 21 B. A scatter plot between the cell-to-cell variation of H3K4me3 and H3K27me3 for clusters annotated as
22 monocytes in bivalent domains (**Methods**).
- 23 C. Cluster-specific bivalent domains associated with H3K4me3 and H3K27me3 were computed for the
24 purpose of finding the relationship between cell-to-cell variation in H3K4me3 and H3K27me3. For each
25 comparison between the H3K4me3 and H3K27me3 clusters, the overlap between cluster-specific
26 bivalent domains was considered, the Spearman's correlation between the coefficient of variation in
27 H3K4me3 and H3K27me3 for these selected bivalent domains was calculated.

Figure 1

A



B

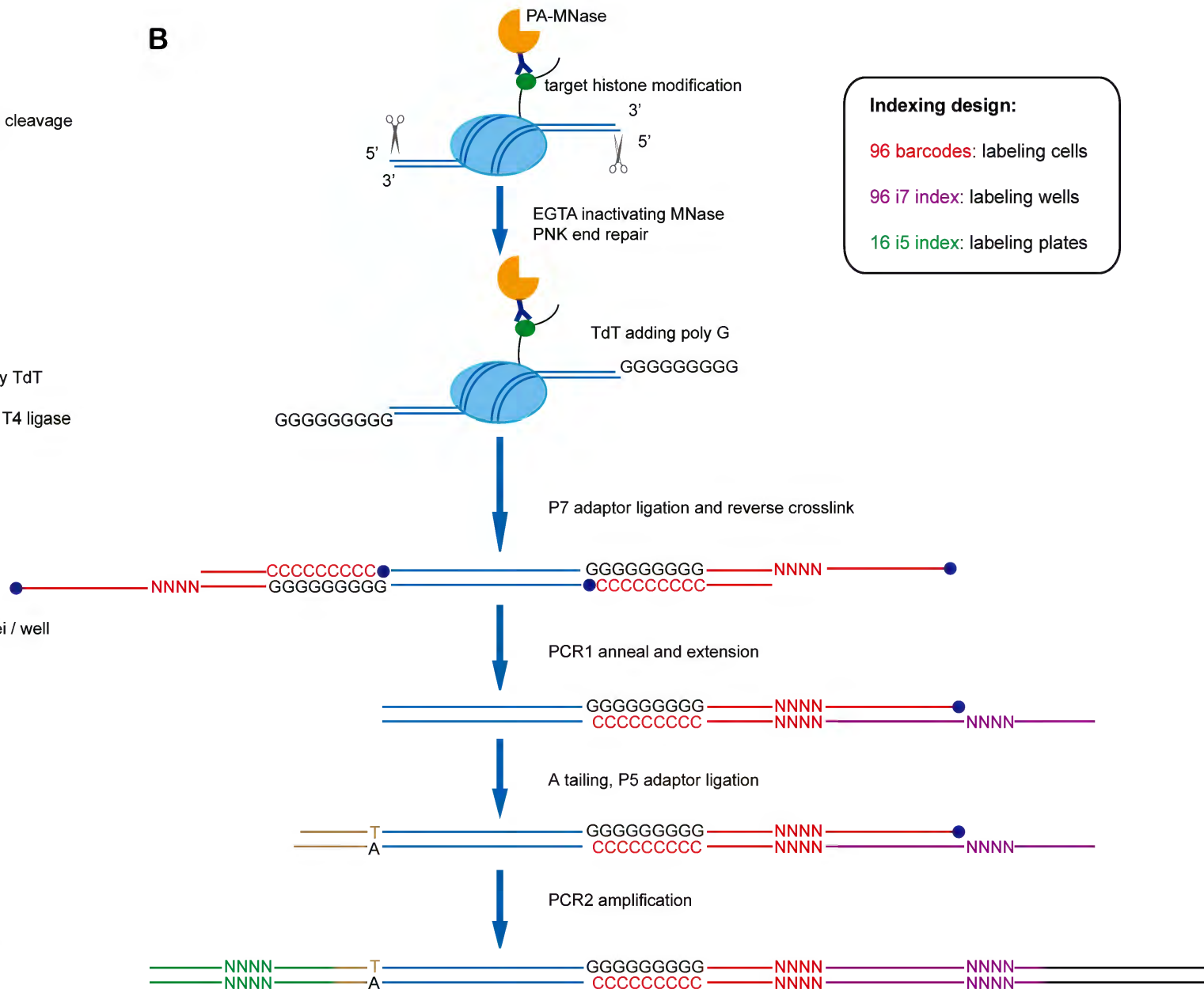


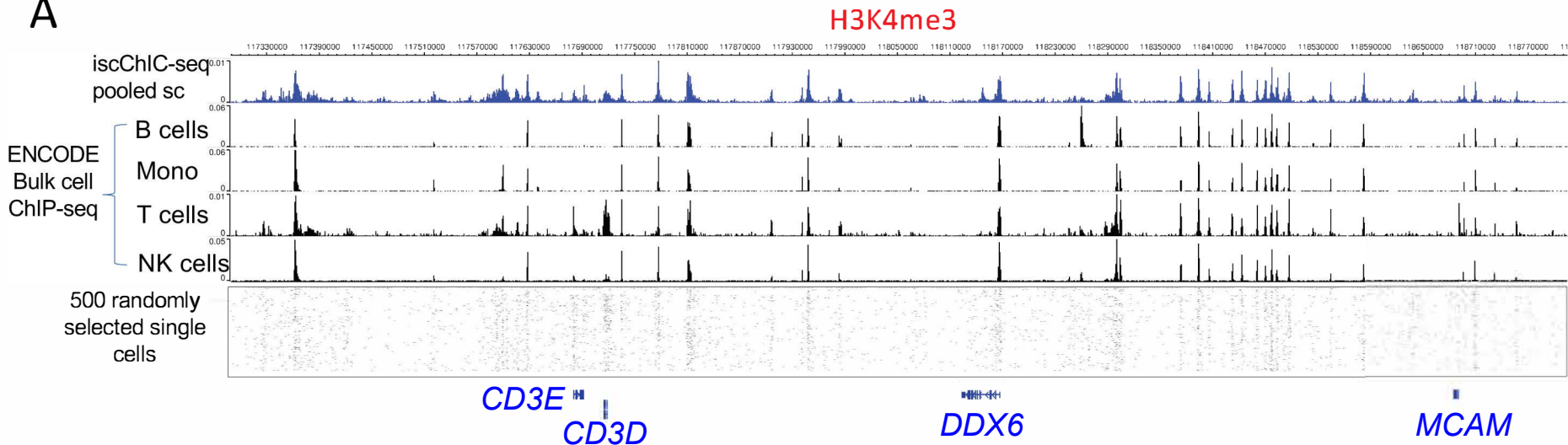
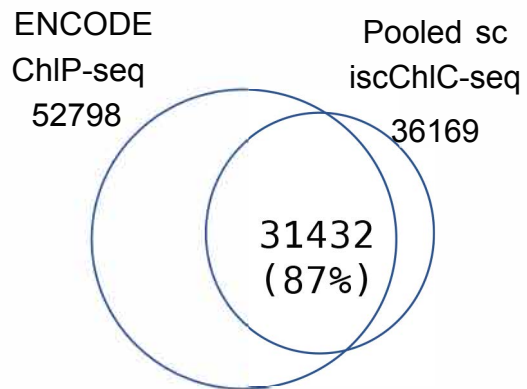
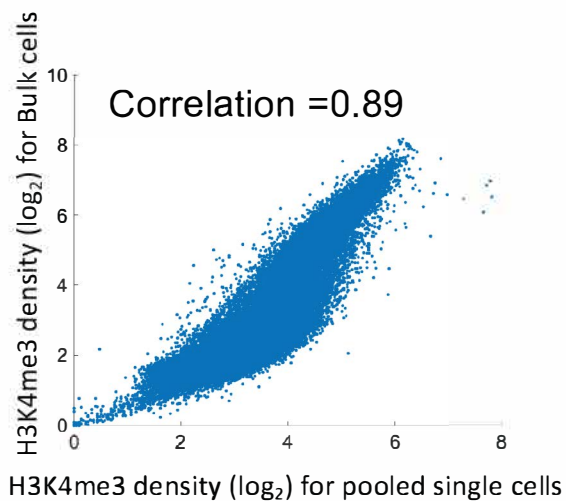
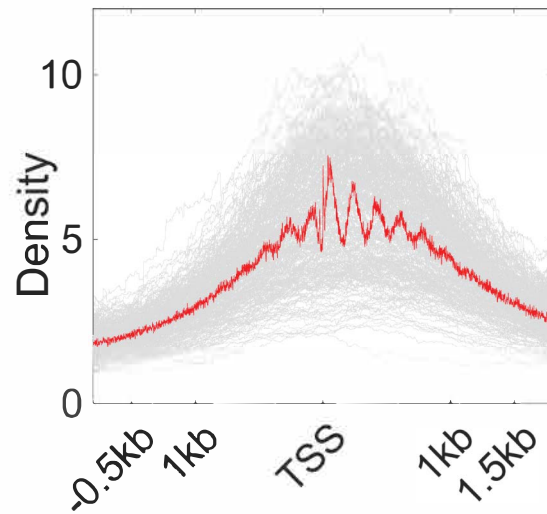
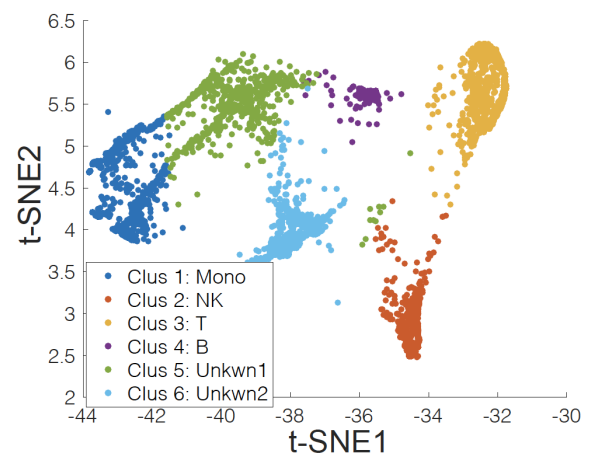
Figure 2**A****B****C****D**

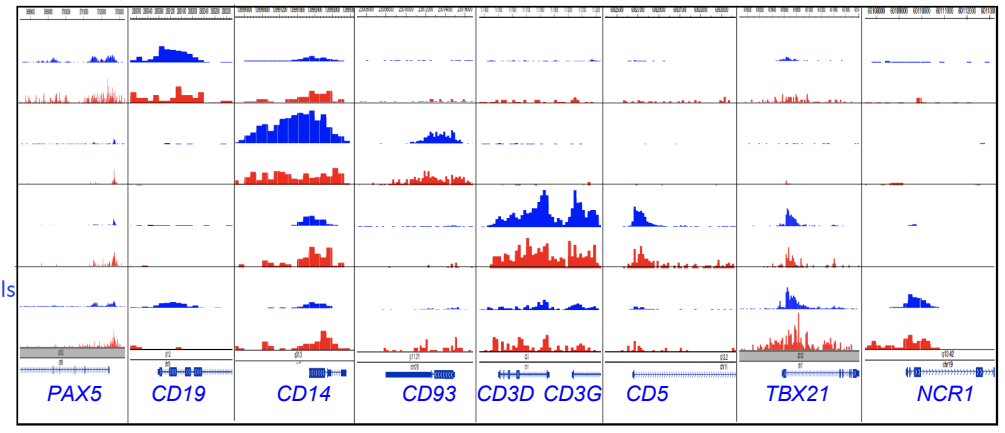
Figure 3

A

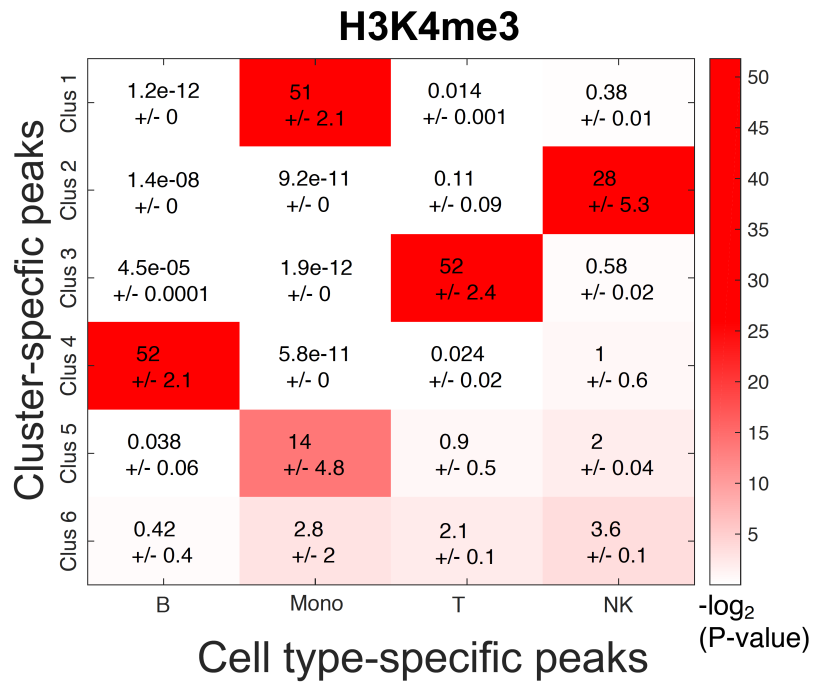


C

ENCODE ChIP-seq B cells
 Pooled single B cells
 ENCODE ChIP-seq Mono
 Pooled single Mono
 ENCODE ChIP-seq T cells
 Pooled single T cells
 ENCODE ChIP-seq NK cells
 Pooled single NK cells



B



D

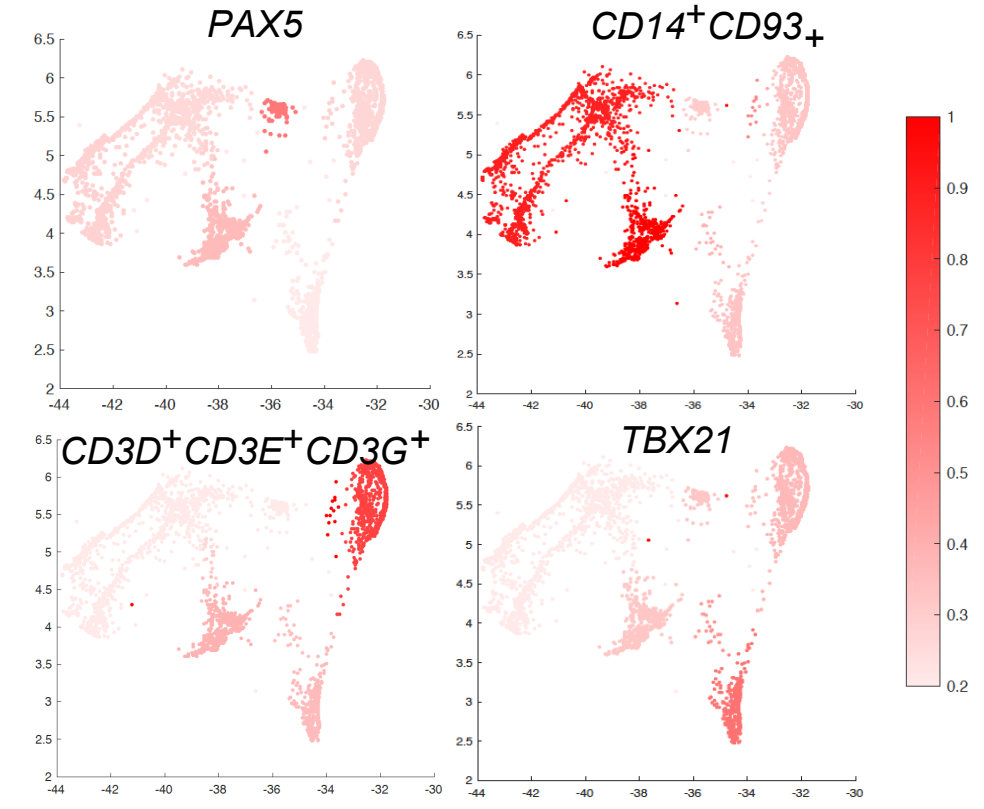
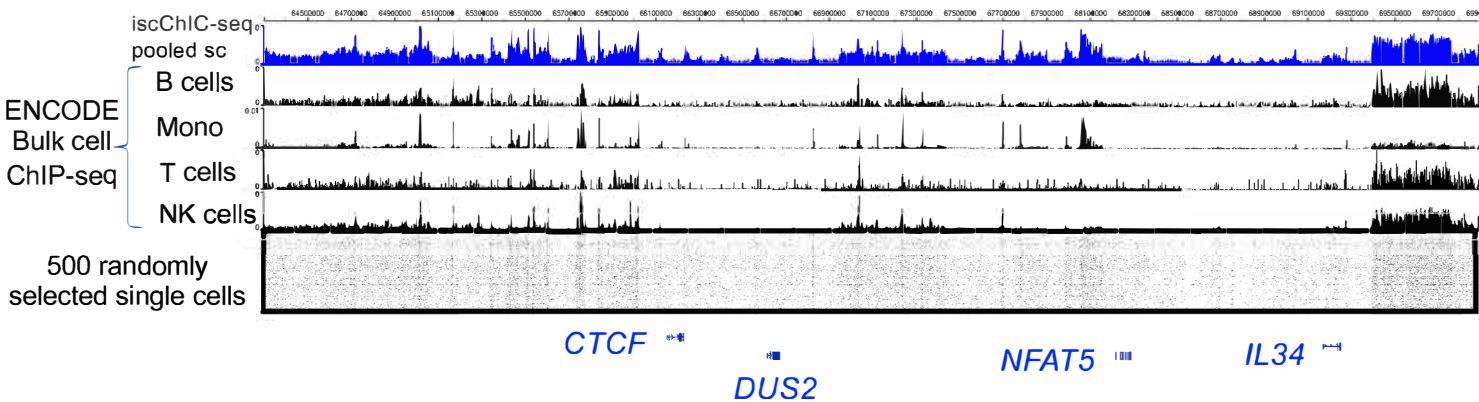
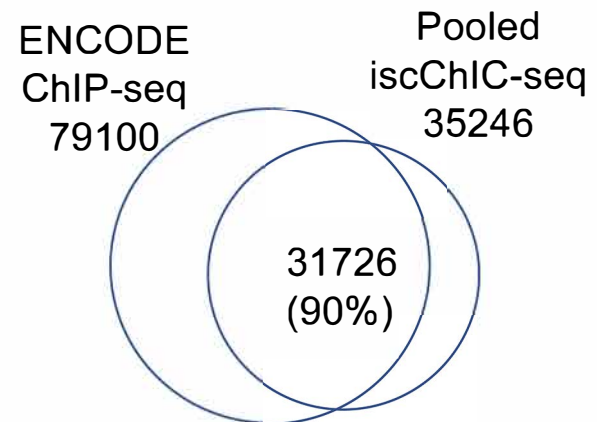


Figure 4

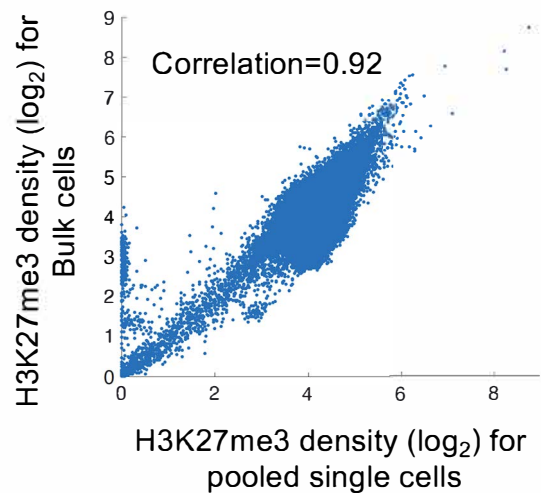
A



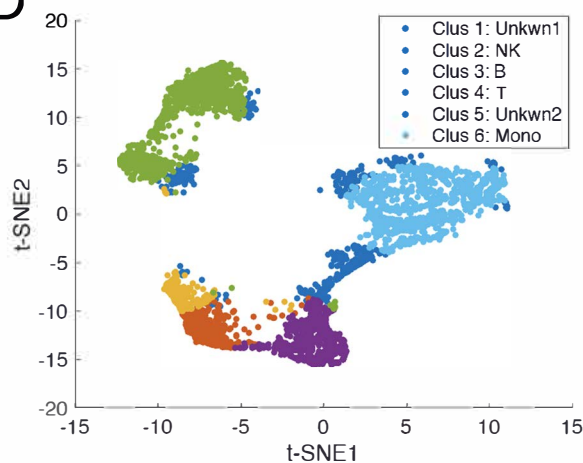
B



C



D



E

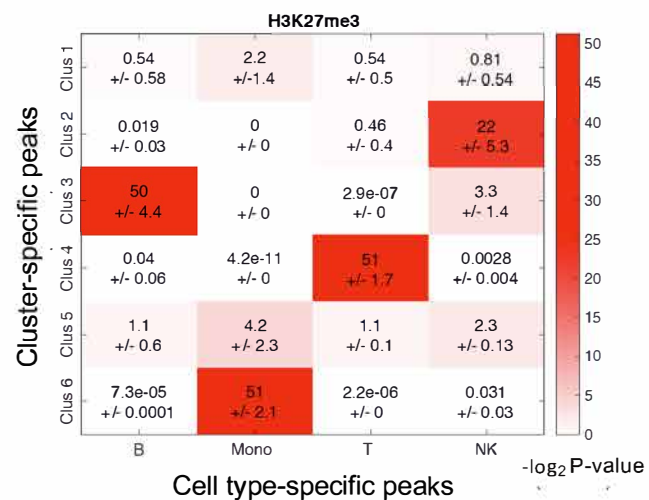
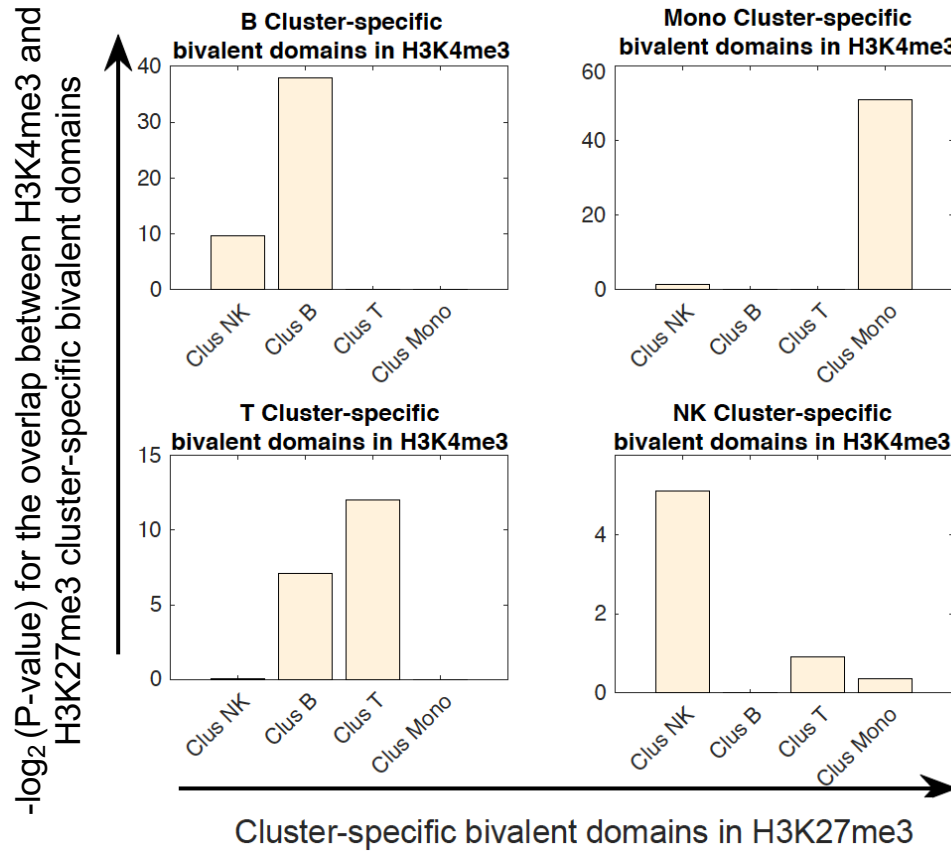
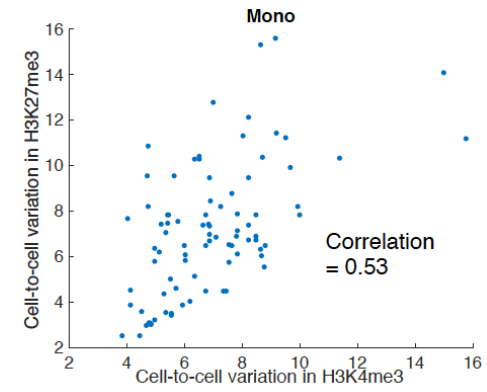


Figure 5

A



B



C

